Article

Not peer-reviewed version

Time-Dependent Theory of Electron Emission Perpendicular to Laser Polarization for Reconstruction of Attosecond Harmonic Beating by Interference of Multiphoton Transitions

Matias L Ocello * , Sebastián David López , Martín Barlari , Diego G. Arbó *

Posted Date: 4 October 2025

doi: 10.20944/preprints202510.0259.v1

Keywords: atomic photoionization; RABBIT; nonperturbative theory; attosecond chronoscopy; phase delays; intrahalfcycle interference

Article

Time-Dependent Theory of Electron Emission Perpendicular to Laser Polarization for Reconstruction of Attosecond Harmonic Beating by Interference of Multiphoton Transitions

Matias L. Ocello [1,2,*], **Sebastián D. López** [3], **Martín Barlari** [1,2] **and Diego G. Arbó** [1,2,4,*]

[1] Institute for Astronomy and Space Physics - IAFE (UBA-CONICET), C1428GA, Buenos Aires, Argentina
[2] Universidad de Buenos Aires, Facultad de Ciencias Exactas y Naturales, Departamento de Física. Buenos Aires, Argentina
[3] Instituto de Investigaciones en Energía No Convencional - INENCO (UNSa - CONICET), Av. Bolivia 5150, 4400, Salta Capital, Argentina
[4] Universidad de Buenos Aires, Ciclo Básico Común, Buenos Aires, Argentina
* Correspondence: mocello@iafe.uba.ar (M.L.O.); diego@iafe.uba.ar (D.G.A.)

Abstract

We present a time-dependent nonperturbative theory of the reconstruction of attosecond beating by interference of multiphoton transitions (RABBIT) for photoelectron emission from hydrogen atoms in the direction perpendicular to the laser polarization axis. Extending our recent semiclassical strong-field approximation (SFA) model developed for parallel emission [López *et al.*, Phys. Rev. A **110**, 013104 (2024)], we derive analytical expressions for the transition amplitudes and demonstrate that the photoelectron probability distribution can be factorized into interhalf- and intrahalfcycle interference contributions, the latter modulating the intercycle pattern responsible for sideband formation. We identify the intrahalfcycle interference between trajectories born within the same half cycle as the mechanism governing attosecond phase delays in the perpendicular geometry. Our results reveal the suppression of even-order sidebands due to destructive interhalfcycle interference, leading to a characteristic spacing between adjacent peaks that doubles the standard spacing observed along the polarization axis. Comparisons with numerical calculations of the SFA and the *ab initio* solution of the time-dependent Schrödinger equation confirm the accuracy of the semiclassical description. This work provides a unified framework for understanding quantum interferences in attosecond chronoscopy, bridging the cases of parallel and perpendicular electron emission in RABBIT-like protocols.

Keywords: atomic photoionization; RABBIT; nonperturbative theory; attosecond chronoscopy; phase delays; intrahalfcycle interference

---

1. Introduction

Attosecond science has opened the way to probe and control electronic dynamics in matter on their natural timescales. Pump–probe techniques combining attosecond extreme-ultraviolet (XUV) pulses with near-infrared (NIR) or visible laser fields provide access to phase and timing information encoded in photoelectron wave packets. Among them, attosecond streaking [1–3] and the reconstruction of attosecond beating by interference of two-photon transitions (RABBIT) [4,5] have become the cornerstone of attosecond chronoscopy of photoionization processes in atoms [6–11], molecules [12], and solids [3,13,14]. While streaking can be interpreted classically as an energy shift induced by the probe field [8,15–19], RABBIT is understood as a quantum interferometer arising from multiple indistinguishable pathways leading to the same final continuum state [7,8].

Most theoretical descriptions of RABBIT rely on perturbative treatments of the probe field, which assume that only two-photon processes dominate and that the probe field intensity is weak enough not to alter the ionization dynamics [20–22]. However, continuum–continuum transitions induced

Preprints.org (www.preprints.org) | NOT PEER-REVIEWED | Posted: 4 October 2025 doi:10.20944/preprints202510.0259.v1

by the probe are intrinsic to the measurement process and cannot be neglected. Nonperturbative approaches based on the strong-field approximation (SFA) [16,23–29] have been successfully employed to extend RABBIT beyond the perturbative regime, allowing the inclusion of multiple probe photons and allowing the identification of different interfering electron trajectories responsible for the observed phase delays. In our recent work [21], we developed a semiclassical time-dependent nonperturbative model within the SFA to describe electron emission in a RABBIT-like scheme along the polarization direction. We demonstrated that the photoelectron probability can be factored into intracycle and intercycle contributions, and we identified the intracycle interference as the main mechanism governing the phase delays.

Angle-resolved studies of laser-assisted photoionization emission (LAPE) have revealed rich interference structures beyond the polarization axis [30]. In particular, photoelectron emission in the perpendicular direction exhibits a distinct interference pattern [31]. This leads to a natural factorization of the spectrum into intrahalfcycle and interhalfcycle contributions, which modulate the well-known intercycle interference responsible for sideband formation. Unlike the case of parallel emission [22], perpendicular emission shows destructive interference between half cycles for the absorption and emission of even numbers of NIR photons, resulting in the suppression of certain sidebands and the double of the characteristic energy spacing between neighboring peaks [31–34]. These features highlight the crucial role of symmetry and emission geometry in determining the structure of the photoelectron spectrum (PES).

In this paper, we extend the nonperturbative time-dependent SFA-based theory of RABBIT developed in [21] to the case of photoelectron emission perpendicular to the laser polarization axis. We demonstrate that our approach provides a unified semiclassical framework for understanding perpendicular emission in RABBIT-like protocols. We obtain an analytical factorization of the photoelectron momentum distribution into intrahalfcycle and interhalfcycle interference contributions. We also demonstrate that the intrahalfcycle interference is directly responsible for the attosecond phase delays. This work thus bridges previous studies on parallel [21] and perpendicular [31] emission, offering new insights into the role of quantum interferences in attosecond chronoscopy.

The paper is organized as follows: In Section 2, we describe the semiclassical model (SCM) used to calculate the photoelectron spectra for the case of perpendicular emission to the polarization direction of the laser in the RABBIT protocol. In Section 3, we present the results and discuss the SCM compared to the SFA and the *ab initio* solution of the time-dependent Schrödinger equation (TDSE) [35–37]. Concluding remarks are presented in Section 4. Atomic units are used throughout the paper, except when otherwise stated.

2. Theory and Methods

We study the ionization of an atomic system interacting with an external laser field in the single-active-electron (SAE) approximation. The TDSE reads

$$i\frac{\partial}{\partial t}|\psi(t)\rangle = \Big[H_0 + H_{\text{int}}(t)\Big]|\psi(t)\rangle, \tag{1}$$

where $H_0 = \vec{p}^2/2 + V(r)$ is the time-independent atomic Hamiltonian, whose first term corresponds to the electron kinetic energy and the second term to the electron-core Coulomb interaction. The laser-atom coupling, referred as the interaction Hamiltonian H_{int} on the right-hand side of Equation (1) produces the promotion of the initially bound electron in the atomic state $|\phi_i\rangle$ to the continuum final state $|\phi_f\rangle$ with energy $E = k^2/2$ and final momentum $\vec{k}$. The final photoelectron momentum distributions can be computed as

$$\frac{dP}{d\vec{k}} = |T_{if}|^2 \tag{2}$$

where T_{if} is the transition amplitude $\phi_i \to \phi_f$.

Within time-dependent distorted wave theory, the transition amplitude in the prior form can be expressed as [25,38]

$$T_{if} = -i \int_{-\infty}^{+\infty} dt \, \langle \chi_f^-(\vec{r},t) | H_{\text{int}}(\vec{r},t) | \phi_i(\vec{r},t) \rangle, \tag{3}$$

where $\phi_i(\vec{r},t) = \varphi_i(\vec{r}) e^{iI_p t}$ is the initial atomic state, I_p the ionization potential, and $\chi_f^-(\vec{r},t)$ is the distorted final state. Within the SFA, the Coulomb distortion in the final channel produced by the ejected-electron state due to its interaction with the residual ion is neglected, thus, the distorted final state can be written as the Volkov function [39], i.e., $\chi_f^- = \chi_f^V$, which is the solution of the Schrödinger equation for a free electron in an electromagnetic field.

For simplicity, in this work, we consider photoionization of a hydrogen atom due to a short train of XUV pulses formed by two consecutive odd high-order harmonics (HH) assisted by a near-infrared (NIR) laser with fundamental frequency ω. The present study can be easily generalized to any atom within the SAE approximation. Both HHs and the NIR laser are linearly polarized in the same direction, i.e., $\vec{F}(t) = F(t)\hat{z}$, where

$$\begin{aligned} F(t) = f_0(t) F_0 \cos(\omega t + \phi) \quad &+ \quad f_{m-1}(t) F_{m-1} \cos[(2m-1)\omega t + \phi_{m-1}] \\ &+ \quad f_m(t) F_m \cos[(2m+1)\omega t + \phi_m], \end{aligned} \tag{4}$$

where $f_0(t)$, $f_{m-1}(t)$, and $f_m(t)$ are functions between 0 and 1 that mimic the corresponding pulse envelopes, F_0, F_{m-1}, and F_m are the field strengths of the NIR and HHs lasers, respectively. Each harmonic undertakes a phase ϕ_{m-1} and ϕ_m, while the NIR takes a phase ϕ. For a long pulse with an adiabatic switch on and off, the vector potential $\vec{A}(t) = -\int_{-\infty}^{t} dt' \vec{F}(t')$ can be written in its central part as

$$\vec{A}(t) \simeq -\frac{f_0(t)}{\omega} F_0 \sin(\omega t + \phi) \, \hat{z}, \tag{5}$$

where we have supposed that the harmonic intensity compared to the intensity of the fundamental laser field fulfills $F_m \ll F_0(2m+1)$ for high harmonic orders, i.e., $m \gg 1$. Therefore, the vector potential of the two HHs can be neglected.

In the present work, we restrict the photoelectron momentum to the direction perpendicular to the polarization axis, i.e., $\vec{k} = k\hat{\rho}$ (in cylindrical coordinates). We analyze similarities and differences with the case of emission parallel to the polarization axis, i.e., $\vec{k} = k\,\hat{z}$, studied recently in [21]. As we use the length gauge in the present work, i.e., $H_{\text{int}}(\vec{r},t) = \vec{r} \cdot \vec{F}(t)$, then from Equation (4), the transition matrix T_{if} in Equation (3) is separable in the different laser fields, i.e., $T = T_0 + T_{m-1} + T_m$, with

$$T_m = F_m \int_{-\infty}^{+\infty} \ell_m(t) \, e^{i[S_m(t) - \phi_m]} \, dt, \tag{6}$$

where

$$\ell_m(t) = -\frac{i}{2} f_m(t) \, \hat{z} \cdot \vec{d}\left[\vec{k} + \vec{A}(t)\right], \tag{7}$$

and

$$S_m(t) = -\int_t^{\infty} dt' \left\{ \frac{\left[\vec{k} + \vec{A}(t')\right]^2}{2} + I_p - (2m+1)\omega \right\}, \tag{8}$$

with the dipole moment defined as $\vec{d}(\vec{v}) = (2\pi)^{-3/2} \langle e^{i\vec{v}\cdot\vec{r}} | \vec{r} | \varphi_i(\vec{r}) \rangle$, and $S_m(t)$ is the generalized classical action for the harmonic frequency $(2m+1)\omega$, i.e., HH$(2m+1)$. With the appropriate choice of the NIR and XUV laser parameters considered, we can assume that the energy domain of the LAPE processes due to HH$(2m+1)$ and HH$(2m-1)$ is well separated from the domain of ionization by an NIR laser alone. Therefore, we can neglect the contribution of NIR ionization T_0 with respect to the contribution of the XUV pulse train. We justify this assumption in the next section. In Equation (6), we have considered the high-frequency time-dependent ionization amplitude due to HH$(2m+1)$ as a single photon absorption transition of energy $(2m+1)\omega$, i.e., the rotating-wave approximation [21,22,30,31]. In the flat-top region of the vector potential in Equation (5), i.e., $f_0(t) = 1$, the time integration in Equation (8) can be analytically calculated, i.e.,

$$S_m(t) = a_m t - \frac{U_p}{2\omega}\sin(2\omega t + 2\phi), \tag{9}$$

where $a_m = k^2/2 + I_p + U_p - (2m+1)\omega$, and $U_p = (F_0/2\omega)^2$ define the electron ponderomotive energy under the fundamental frequency NIR electric field.

The RABBIT protocol can be thought of as a special case of LAPE, in which a pulse train formed of several high-harmonic fields is responsible for the ionization of the target. For the sake of simplicity, we consider atomic ionization by only two neighboring odd high-harmonics (HH) of frequencies $(2m-1)\omega$ and $(2m+1)\omega$, HH$(2m-1)$ and HH$(2m+1)$, respectively, followed by continuum-continuum transitions due to the action of the fundamental frequency ω. In this sense, the transition probability from the initial atomic bound state to the continuum can be thought of as the coherent superposition of the individual contributions of every HH, i.e.,

$$|T|^2 = |T_{m-1} + T_m|^2, \tag{10}$$

where T_m is given in Equation (6). The case of a single contributing HH has already been studied, showing that the phase ϕ is not important, affecting the photoelectron spectrum only through boundary conditions of the short XUV pulse [22,30,31]. Instead, in the RABBIT protocol, the phases of each of the two transition amplitudes T_{m-1} and T_m in Equation (10) do matter. In RABBIT, the addition of various high-frequency components (two in this case) in the pump field breaks the translational invariance in the time domain present in ionization by only one HH and, thus, an origin can be established for the reference frame of the relative phase of the probe [21]. Therefore, the ionization probability [Equation (10)] depends on the relative phases ϕ, ϕ_{m-1}, and ϕ_m in Equation (4).

If we consider that the central part of the NIR envelope field that does not vary starts at $t=0$, the square of the vector potential in Equation (5) is periodic every half cycle, i.e., $A^2(t + j\pi/\omega) = A^2(t)$, or equivalently, $\vec{A}(t + j\pi/\omega) = (-1)^j \vec{A}(t)$, with j any positive integer number, as well as the square of the dipole moment, i.e., $d^2\left[\vec{k} + \vec{A}(t + j\pi/\omega)\right] = d^2\left[\vec{k} + \vec{A}(t)\right]$, or equivalently, $\vec{d}\left[\vec{k} + \vec{A}(t + j\pi/\omega)\right] = (-1)^j \vec{d}\left[\vec{k} + \vec{A}(t)\right]$ (see appendix A). Besides, we observe that the second term of the right hand side of Equation (9) is a time-oscillating function with half the period of the fundamental laser field (π/ω), i.e.,

$$S_m(t + j\frac{\pi}{\omega}) = S_m(t) + \frac{j\pi a_m}{\omega}. \tag{11}$$

The integration domain of Equation (6) extends to the non-zero values of the envelope $f_m(t)$, for simplicity $\tau = 2\pi N/\omega$, with N any real positive number. However, we particularize our analysis for semi-integer values of N. Thus, we can rewrite the transition matrix T_m due to the contribution of HH$(2m+1)$ in Equation (6) as the addition of N optical laser cycles of the fundamental probe field, i.e.,

$$\begin{aligned} T_m &= F_m \int_0^{2\pi N/\omega} \ell_m(t) e^{i[S_m(t) - \phi_m]}\, dt \\ &= F_m e^{-i\phi_m} \sum_{j=0}^{N-1} \int_{2\pi j/\omega}^{2\pi(j+1)/\omega} \ell_m(t) e^{iS_m(t)} dt. \end{aligned} \tag{12}$$

By performing the transformation $t = t' + j2\pi/\omega$, the temporal integral in the second line of Equation (12) becomes delayed in j cycles of the probe laser. Keeping in mind the periodicity of $\ell_m(t)$derived from the periodicity of the dipole element when $f_m(t) = 1$, it is straightforward to factorize the transition amplitude as [40–42]

$$\begin{aligned} T_m &= F_m e^{-i\phi_m} \sum_{j=0}^{N-1} e^{i2\pi a_m j/\omega} \int_0^{2\pi/\omega} \ell_m(t') e^{iS_m(t')} dt' \\ &= F_m e^{-i\phi_m} \frac{\sin\left(a_m \pi N/\omega\right)}{\sin\left(a_m \pi/\omega\right)} e^{i\pi a_m (N-1)/\omega} I_m(k), \end{aligned} \tag{13}$$

where the factor

$$I_m(k) = \int_0^{2\pi/\omega} \ell_m(t') e^{iS_m(t')} dt' \tag{14}$$

in Equation (13) corresponds to the contribution of HH$(2m+1)$ ionization from only one optical cycle of the fundamental field.

For an integer number of cycles N, the factors $\exp[i\pi a_m(N-1)/\omega]$ and $\sin\left(a_m \pi N/\omega\right)/\sin\left(a_m \pi/\omega\right)$ are independent of the harmonic index m. Therefore, they can be factorized in Equation (10) leading to

$$|T|^2 = \underbrace{\left|\frac{\sin\left(a_m \pi N/\omega\right)}{\sin\left(a_m \pi/\omega\right)}\right|^2}_{\texttt{intercycle}} \underbrace{\left|F_{m-1} e^{-i\phi_{m-1}} I_{m-1}(k) + F_m e^{-i\phi_m} I_m(k)\right|^2}_{\texttt{intracycle}}. \tag{15}$$

We manage to split the total transition probability in the RABBIT protocol into the intercycle interference factor [first factor in Equation (15)] and the intracyle interference factor [second factor in Equation (15)] [21,25,41,43]. The zeros of the denominator of the intercycle factor, i.e., $a_m \pi/\omega = n\pi$, correspond to energy values

$$E_{2m\pm1+n} = (2m \pm 1 + n)\omega - I_p - U_p, \tag{16}$$

corresponding to the HH$(2m \pm 1)$ one-photon absorption of frequency $(2m \pm 1)\omega$ followed by the absorption or emission of $|n|$ photons of fundamental frequency ω when n is positive or negative, respectively. Such maxima at energies given by Equation (16) are recognized as the SBs in the PES of the HH$(2m \pm 1)$ in presence of the fundamental laser [21,22,30,31] and they are also the SBs formed by the laser dressed train of pulses composed by the two HH$(2m-1)$ and HH$(2m+1)$. In fact, when the number of cycles of the NIR $N \to \infty$, the intercycle factor satisfies the conservation of energy. Instead, for a finite pump pulse of duration τ (of the order of $2\pi N/\omega$), each sideband has a width $\Delta E \sim \omega/N$, fulfilling the uncertainty relation $\Delta E \tau \sim 2\pi$, where τ is the duration of the pulse. In Figure 1, we have depicted the corresponding SBs as a function of the intensity of the NIR laser, which results in straight lines of negative slope $-U_p/I$. One can observe that their energies are straight lines, since the ponderomotive energy U_p is proportional to the intensity of the NIR laser. In Figure 1 we can observe the SBs' values given by Equation (16) for a combination of values of m and n.

Alternatively, we can regard the intracycle factor $I_m(k)$ in Equation (14) as the separate contribution of the two half cycles

$$I_m(k) = \int_0^{\frac{\pi}{\omega}} \ell_m(t') e^{iS_m(t')} dt' + \int_{\frac{\pi}{\omega}}^{\frac{2\pi}{\omega}} \ell_m(t') e^{iS_m(t')} dt' \tag{17a}$$

$$= 2ie^{i\frac{\pi a_m}{2\omega}} \sin\left[\frac{\pi a_m}{2\omega}\right] J_m(k) \tag{17b}$$

where in the second term of the right hand side of Equation (17a) we have performed the substitution $t'' = t' - \pi/\omega$ and used the periodicity properties of $\ell_m(t)$ and $S_m(t)$ to arrive at Equation (17b). The factor $\sin[\pi a_m/(2\omega)]$ in Equation (17b) corresponds to the interference between the ionization during the first and second half cycles of only one optical cycle of the NIR laser and its square is called as the interhalfcycle interference pattern which cancels at $a_m = n\omega$ with $|n| = 0, 2, 4, \ldots$. This excludes the exchange of an even number NIR laser photons in LAPE or, equivalently, $|n|$ must be odd in Equation

(16). Therefore, SBs with even number of exchanged photons in Figure 1 in dotted-dashed light blue (grey) become frustrated due to the inter-half-cycle interference. The last factor in Equation (17b) corresponds to the ionization amplitude due to HH$(2m+1)$ occurring during only one half cycle pulse of the NIR and is defined as

$$J_m(k) = \int_0^{\frac{\pi}{\omega}} \ell(t')e^{iS_m(t')}dt'. \tag{18}$$

Taking into account Equations (17a) and (18), the transition probability of LAPE corresponding to HH$(2m+1)$ becomes

$$\begin{aligned} T_m &= 2ie^{i\pi a_m(N-1/2)/\omega}F_m e^{-i\phi_m}\frac{\sin(a_m\pi N/\omega)}{\sin(a_m\pi/\omega)}\sin[\pi a_m/(2\omega)]\, J_m(k) & \text{(19a)}\\ &= ie^{i\pi a_m(N-1/2)/\omega}F_m e^{-i\phi_m}\frac{\sin(a_m\pi N/\omega)}{\cos[a_m\pi/(2\omega)]}J_m(k). & \text{(19b)}\end{aligned}$$

It is easy to show that when the duration of both laser fields of HH$(2m-1)$ and HH$(2m+1)$ are a semi-integer number of half cycles of the NIR laser, i.e., $\tau = 2\pi N/\omega$ with $N = 1/2, 1, 3/2, 2, 5/2, \ldots$, the factor $\exp[i\pi a_{m-1}(N-1/2)/\omega]\sin(a_{m-1}\pi N/\omega)/\cos[a_{m-1}\pi/(2\omega)]$ is independent of the HH index m, which means that it can be factorized in Equation (10) as

$$|T|^2 = \underbrace{\left(\frac{\sin(a_m\pi N/\omega)}{\cos[a_m\pi/(2\omega)]}\right)^2}_{\texttt{interhalfcycle}}\underbrace{\left|F_{m-1}e^{-i\phi_{m-1}}J_{m-1}(k) + F_m e^{-i\phi_m}J_m(k)\right|^2}_{\texttt{intrahalfcycle}}. \tag{20}$$

Equation (20) indicates that the photoelectron spectrum can be factorized as the contribution of photoionization released at different half cycles (*interhalfcycle* interference) described by the first factor and the contribution within the same (any) half cycle (*intrahalfcycle* interference), governed by the second factor. So far, it is worth to mention that factorizations into interhalf- and intrahalfcycle [Equation (20)] or inter- and intracycle interferences [Equation (15)] are direct consequences of the time symmetries of the problem and rely only on the SFA.

We can compute $J_m(k)$ either numerically, whose result we call SFA, or analytically, by using the saddle-point approximation, which is the cornerstone of the SCM, i.e.,

$$J_m(k) = \sum_{\alpha=1}^{2} g_m(k, t^{(\alpha)})\left[iS_m(t^{(\alpha)}) + i\frac{\pi}{4}\mathrm{sgn}[\ddot{S}_m(t^{(\alpha)})]\right], \tag{21}$$

where the saddle times $t^{(\alpha)}$ and the weighting factor $g_m(k, t^{(\alpha)})$ are found in the appendix B. In Figure 1 we plot the classical allowed regions for the LAPE ionization from HH29 and HH31, observing an overlap between them, which conforms to the classical allowed region in our non-perturbative SCM for RABBIT (see Appendix B). The minimum value of the classical allowed region for RABBIT corresponds to $U_P = \omega$, which, for $\omega = 0.05$ a.u., corresponds to $I_{\min} = 1.7 \times 10^{13}$ W/cm^2, which is shown in Figure 1 with the vertical left dotted line.

To evaluate the action $S_m(t^{(\alpha)})$ at the ionization times in Equation (9), we can consider the accumulated action $\Delta S_m = S_m(t^{(2)}) - S_m(t^{(1)})$ between the two ionization times and the average action $\bar{S}_m = [S_m(t^{(1)}) + S_m(t^{(2)})]/2$. Therefore, $J_m(k)$ can be written as

$$J_m(k) = 2g_m(k)e^{i\bar{S}_m}\gamma_m(k), \tag{22}$$

where the factor $\gamma_m(k)$ is given by

$$\gamma_m(k) = \begin{cases} \cos\left(\frac{\Delta S_m}{2} - \frac{\pi}{4}\right), & \text{if } A(t^{(1)})A(t^{(2)}) \geq 0, \\ \sin\left(\frac{\Delta S_m}{2} - \frac{\pi}{4}\right), & \text{if } A(t^{(1)})A(t^{(2)}) < 0. \end{cases} \tag{23}$$

Summing up, within the SCM, the RABBIT transition probability to the continuum can be written as

$$|T|^2 = \underbrace{\left| \frac{\sin\left(\frac{\pi a_m N}{\omega}\right)}{\cos\left(\frac{\pi a_m}{2\omega}\right)} \right|^2}_{\texttt{interhalfcycle}} \underbrace{\left| F_{m-1} e^{-i\phi_{m-1}} g_{m-1}(k) e^{i\bar{S}_{m-1}} \gamma_{m-1}(k) + F_m e^{-i\phi_m} g_m(k) \gamma_m(k) e^{i\bar{S}_m} \right|^2}_{\texttt{intrahalfcycle}}, \tag{24}$$

where the average action fulfills $\bar{S}_m = -\, n(\phi - f_m)$ with f_m a constant multiple of $\pi/2$. For perpendicular emission, f_m is independent of the laser intensity, unlike the parallel case [21]. In Figure 2a we plot the interhalfcycle interference factor in the solid orange line. We observe that even values of exchanged NIR photons n are precluded so that we can name even SBs as frustrated SBs. This characteristic applies not only to the RABBIT protocol, but also to LAPE and photoionization in the perpendicular direction [31–34]. In Figure 2b, the intrahalfcycle interference factor modulates the intracycle pattern, which, in turn, modulates the total ionization probability. The small peaks at $E \simeq 0.77$ and 0.8 correspond to the incipient SB with $n = 0$, which is suppressed by interhalfcycle interference. In Figure 2a we plot the intercycle factor as a function of the photoelectron energy for $N = 2$, showing the SB energy peaks of width ΔE and positions given by Equation (16). In Figure 2b, the intracycle interference pattern for $N = 1$ and the total pattern for $N = 2$ are shown in red and black lines. One can observe that the intracycle pattern for $N = 1$ modulates the corresponding PES to $N = 2$. This result was already observed for forward emission in the RABBIT protocol [21]. In the following, we point out the differences between forward and perpendicular emission.

We now focus on the phase of the probability amplitude for each SB for energies very close to any sideband [Equation (16)] when the values of $a_m \simeq n\omega$ and the total amplitude in Equation (24) can be written as

$$|T^{(n)}|^2 = 4N^2 \left| F_{m-1} g_{m-1}^{(n+2)} e^{-i\phi_{m-1}} e^{-i\phi} \tilde{\gamma}_{m-1}^{(n+2)} + F_m g_m^{(n)} e^{-i\phi_m} e^{i\phi} \tilde{\gamma}_m^{(n)} \right|^2 \tag{25}$$

where we have defined $\tilde{\gamma}_m^{(n)} = e^{inf_m} \gamma_m^{(n)}$, $g_m^{(n)} = g_m(k)$ correspond to energies $k^2/2 = E_{2m+1+n}$ in Equation (16).

Taking into account Equation (25), the transition probability to a specific SBn can be written as

$$\left| T^{(n)} \right|^2 = A + B\cos(2\phi + \delta), \tag{26}$$

where A and B depend on each contribution and δ is the phase delay given by (see Appendix B of [21] for a detailed calculation),

$$\delta = \underbrace{\phi_m - \phi_{m-1}}_{\texttt{HH}} + \underbrace{\arg\left[\tilde{\gamma}_m^{(n)}\right] - \arg\left[\tilde{\gamma}_{m-1}^{(n+2)}\right]}_{\texttt{atomic}}. \tag{27}$$

The first two terms of the phase delay δ in Eq (27), $\phi_m - \phi_{m-1}$, correspond to the difference in group delays of HH($2m+1$) and HH($2m-1$) of the XUV field when arriving at the target, whereas the last two terms correspond to atomic delays within the SFA. In our SCM of RABBIT, the population of every SB is the result of the interference of two different contributions with a multitude of quantum paths each one, not just the two photon transitions considered at lowest perturbative order of the NIR intensity [4,7,44–46].

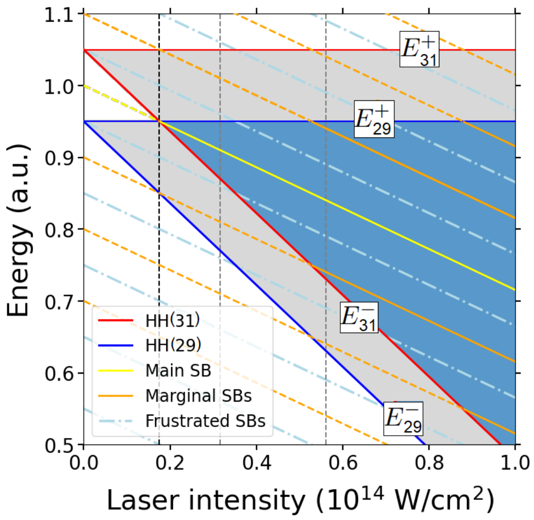

Figure 1. Schematic spectrogram in the energy domain for ionization of HH29 and HH31 as a function of the NIR laser intensity. The classically allowed region for each harmonic: $E_{2m+1}^{-} < E < E_{2m+1}^{+}$ ($m = 14$ and 15) is shaded in light gray whereas the overlap of the two classically allowed regions: $E_{2m+1}^{-} < E < E_{2m-1}^{+}$ ($m = 15$) is shaded in blue. The upper classical limits E_{2m+1}^{+} are independent of the NIR laser intensity and the lower classical limits E_{2m+1}^{-} exhibits a slope of $-2U_p/I$. The white area represents classically forbidden regions. HH29, HH31, and all SBs are drawn as straight lines of slope given by $-U_p/I$. Full lines correspond to observed (odd) SBs, whereas doted-dashed lines to forbidden (even) SBs. The left vertical dashed line indicates the minimum NIR intensity into the classical allowed region for the two harmonics HH29 and HH31: $I \simeq 1.75 \times 10^{13}$ W/cm^2 ($F_0 = 0.0224$ a.u.). The other two vertical dashed lines indicate the two NIR intensity values analyzed in the text: $I \simeq 3.16 \times 10^{13}$ W/cm^2 ($F_0 = 0.03$ a.u.) and $I \simeq 5.62 \times 10^{13}$ W/cm^2 ($F_0 = 0.04$ a.u.). The NIR laser frequency is $\omega = 0.05$ a.u., and the HH29 and HH31 frequencies are $29\omega = 1.45$ a.u. and $31\omega = 1.55$ a.u., respectively. $I_p = 0.5$ a.u. (atomic hydrogen)

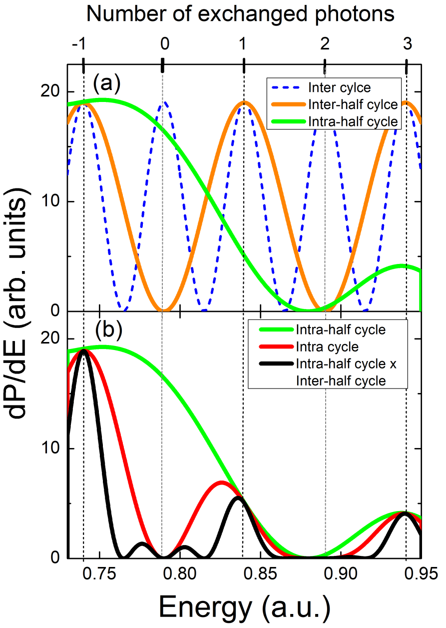

Figure 2. Buildup of the interference pattern in the perpendicular direction following the SCM for $N = 2$. (a) Intrahalfcycle interference pattern in thick green line, intercycle pattern in thin dotted blue line, and interhalfcycle pattern given in thin orange line [see Equations (15) and (24)]. (b) Intracycle pattern in thick green line, total interference pattern in black line [see Equations (15) and (24)]. The intracycle pattern is shown in red line. Vertical lines depict the energy positions of the SBs with odd $|n|$ in Equation (16). The NIR laser intensity is $I \simeq 5.62 \times 10^{13}$ W/cm^2 ($F_0 = 0.04$ a.u.), where the rest of the laser parameters are the same as in Figure 1. The relative phase and $\phi = 0$ with $\phi_{m-1} = \phi_m$.

doi:10.20944/preprints202510.0259.v1

3. Results and Discussions

In order to probe the general result that the ionization probability of photoelectrons emitted perpendicularly to the polarization axis of the train of XUV pulses and the NIR laser pulse can be factorized in two different ways—namely, into intracycle and intercycle interferences [Equation (15)] or into intrahalf- and interhalfcycle interferences [Equation (24)]—we compare the photoelectron spectrum $dP/dE = 2\pi\sqrt{2E}\,|T_{if}|^2$ within the SCM, the SFA, and the *ab initio* numerical solutions of the TDSE. The NIR and XUV frequencies are taken as $\omega = 0.05$ a.u. and $\omega_{2m+1} = (2m+1)\omega$, respectively, with $m = 14$ and 15. We consider the NIR laser duration be $8\pi/\omega$, corresponding to four optical cycles, and three different durations of the XUV pulse train, $\tau = \pi/\omega$, $2\pi/\omega$, and $4\pi/\omega$, corresponding to $N = 1/2, 1$, and 2 optical cycles of the NIR laser, all of them starting right after the second cycle of the NIR laser, saving the first cycle for a linear ramp on and the fourth cycle for a linear ramp off. The envelopes $f_m(t)$ are defined in the same way: a flat-top unitary region with a one-cycle linear ramp on and a one-cycle linear ramp off.

Figure 3 shows the results of the SFA and the TDSE for the same XUV and NIR pulse parameters as in Figure 2, with $F_{m-1} = F_m = 0.1$ a.u. and $F_0 = 0.03$ a.u. ($I \simeq 3.16 \times 10^{13}$ W/cm^2 in panels a and c) and $F_0 = 0.04$ a.u. ($I \simeq 5.62 \times 10^{13}$ W/cm^2 in panels b and d), for relative phases $\phi_{m-1} = \phi_m$ and $\phi = 0$. The agreement between the PES along the perpendicular direction calculated with SFA and TDSE is remarkable, and complements their comparison with the SCM results in Figure 2b. Several conclusions can be drawn. First, the negligible effect of the Coulomb potential of the residual ion on the electron yield is evidenced by the almost perfect agreement between the SFA and TDSE spectra evidences. A more detailed analysis of Coulomb effects in RABBIT spectra will be presented in a forthcoming work. Second, the factorization of perpendicular photoelectron emission into either intra- and intercycle interference patterns [Equation (15)] or intra- and interhalfcycle interference patterns [Equation (24)] is validated not only in the SCM and SFA spectra but also in the full TDSE results. Figure 3 shows that the intrahalfcycle interference pattern, calculated as the energy distribution for a XUV pulse duration of half a laser cycle, i.e., $\tau = \pi/\omega$, modulates the intracycle interference pattern, calculated as the energy distribution for a XUV pulse duration of one laser cycle, i.e., $\tau = 2\pi/\omega$, as predicted in Equation (24). In the same way, the intracycle interference factor modulates the SBs in the energy distribution for a longer XUV pulse, i.e., $\tau = 4\pi/\omega$. When the XUV pulse duration involves several periods of the laser, i.e., $\tau = 4\pi/\omega$, the positions of the SBs in the SFA and TDSE calculations in Figure 4 agree with the SCM expressed in Equation (16) for odd number $|n|$ of exchanged NIR photons as described in the previous section. Conversely, SBs with an even number $|n|$ of exchanged NIR photons are suppressed by the destructive interference between XUV emission during each first and second half cycles of all the cycles of the NIR laser involved. SFA and TDSE PES extend beyond the classical upper limits $E^+_{29} = 0.95$ a.u. and $E^+_{31} = 1.05$ a.u. and beyond the lower limits $E^-_{29} = 0.77$ a.u. (0.63 a.u.) and $E^-_{31} = 0.87$ a.u. (0.73 a.u.) for $I \simeq 3.16 \times 10^{13}$ W/cm^2 ($I \simeq 5.62 \times 10^{13}$ W/cm^2) or $F_0 = 0.03$ a.u. (0.04 a.u.).

We have also investigated the dependence of the perpendicular PES on the intensity of the NIR laser, following the schematic representation in Figure 1. Figure 4 shows the energy distributions calculated with the SCM (a, d, g), the SFA (b, e, h), and the TDSE (c, f, i) for laser intensities up to 10^{14} W/cm^2 ($F_0 = 0.053$ a.u.). The analysis includes different XUV pulse durations, $\tau = \pi/\omega$, $2\pi/\omega$, and $4\pi/\omega$. Figure 2 and Figure 3 correspond to cuts of Figure 4 at $I \simeq 3.16 \times 10^{13}$, W/cm^2 and $I \simeq 5.62 \times 10^{13}$ W/cm^2. By definition, the classical boundaries E^+_{29} and E^-_{31}, shown as dotted lines, delimit the SCM spectrogram in Figure 4a, 4d, and 4g. For $\tau = \pi/\omega$ (first row), the intrahalfcycle interference stripes exhibit a negative slope. For $\tau = 2\pi/\omega$ (second row), the intrahalfcycle interference patterns are flanked by nodes corresponding to the zeros of the interhalfcycle factor in Equation (24). i.e., $4\sin^2\frac{\pi a_m}{2\omega}$ for $N = 2$, which vanishes for $a_m = 2n\omega$, i.e., for all even $|n|$ number of exchanged NIR photons. The slope of maxima (visible SBs) and minima (frustrated SBs) is $7.13 \times 10^{-4}/\omega^2$, where the intensity units are in W/cm^2, and the energy spacing between consecutive minima (and maxima) is 2ω. This result is inherent to all emissions in the perpendicular direction to the polarization of the laser fields, not only for RABBIT and LAPE but also for one-color ionization [32–34]. For $\tau = 4\pi/\omega$ (third column), the sidebands become thinner due to the time–energy uncertainty relation $\Delta E\, \Delta\tau \approx \hbar$, which reflects destructive intercycle interference for energies far from conservation values. The SCM reproduces the characteristic intrahalf- and intracycle interference stripes with negative slope observed in the SFA and TDSE spectrograms, although the quantum results extend beyond the classical boundaries, as expected.

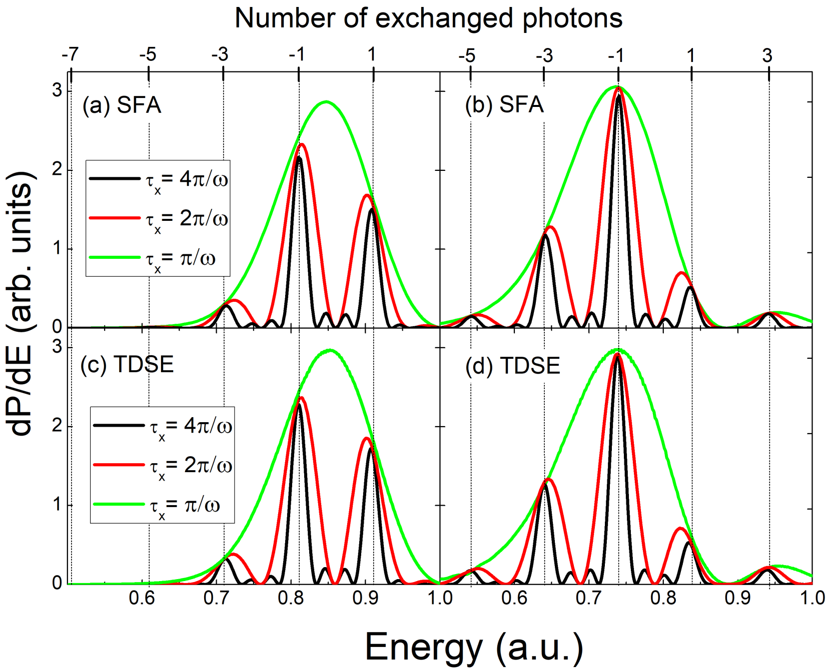

Figure 3. Photoelectron spectra in the perpendicular direction calculated within the SFA (a and b) and the TDSE (c and d), for different XUV pulse durations $\tau_X = \pi/\omega$ (green), $2\pi/\omega$ (red), and $4\pi/\omega$ (black) for two different NIR intensities: $I \simeq 3.16 \times 10^{13}$ W/cm^2 ($F_0 = 0.03$ a.u. in a and c) and $I \simeq 5.62 \times 10^{13}$ W/cm^2 ($F_0 = 0.04$ a.u. in b and d). The XUV peak fields are $F_{m-1} = F_m = 0.1$ and the NIR parameters are the same as in Figure 2. Vertical lines depict the positions of the relevant SBs (odd n) according to Equation (16). The relative phase is $\phi = 0$ and $\phi_{m-1} = \phi_m$. Photoelectron energy distributions have been vertically rescaled for better visualization.

So far, we have analyzed electron emission in the transverse direction for phases $\phi = 0$. To reveal how the intracycle interference pattern changes with the relative phase ϕ, we studied the dependence of the photoelectron spectra as ϕ varies from 0 to 2π. Figure 5a shows the intrahalfcycle interference pattern ($N = 1/2$) calculated within the SCM (for $\tau = \pi/\omega$). We mark the two discontinuities for HH29 and HH31 at energy values $E_{\mathrm{disc},m} = \frac{1}{2}\left[v_{0,m}^2 - A^2(\phi/\omega)\right]$ (see appendix B and [31]. For $\phi = 0$, the discontinuity lies at $E_{\mathrm{disc},m} = v_{0,m}^2/2$, which coincides with the upper classical boundary. As ϕ varies, the discontinuity follows the squared vector potential with π-periodicity in contrast with the 2π-periodicity characteristic of parallel emission [21,22,31]. For $\phi = 0, \pi, 2\pi$, the discontinuity occurs at $E^+_{2m+1} = v_{0,m}^2/2$, while for $\phi = \pi/2, 3\pi/2$, it shifts to $E^-_{2m+1} = v_{0,m}^2/2 - 2U_p$. The intracycle interference ($N = 1$) and total spectra ($N = 2$) shown in Figs. 5d and 5(e) display jumps in the probability distribution at the discontinuities. For $\tau = 2\pi/\omega$, the SCM spectrum (Figure 5d shows horizontal lines corresponding to intracycle interference, i.e., interference between the first and second half cycles, consistent with the factor $\sin^2(\pi a_m/2\omega)$ in Equation (17b). For $\tau = 4\pi/\omega$ (Figure 5g), the SCM spectrum shows intercycle interference modulated by the intracycle pattern, but the discontinuities at the SBs [Equation (16)] are absent. As the SBs narrow, the discontinuities blur. The SFA and TDSE results extend further the classical limits exhibiting more SBs as seen in second and third columns of Figure 5 and agree closely with the SCM within the classical boundaries, validating the time-dependent semiclassical picture.

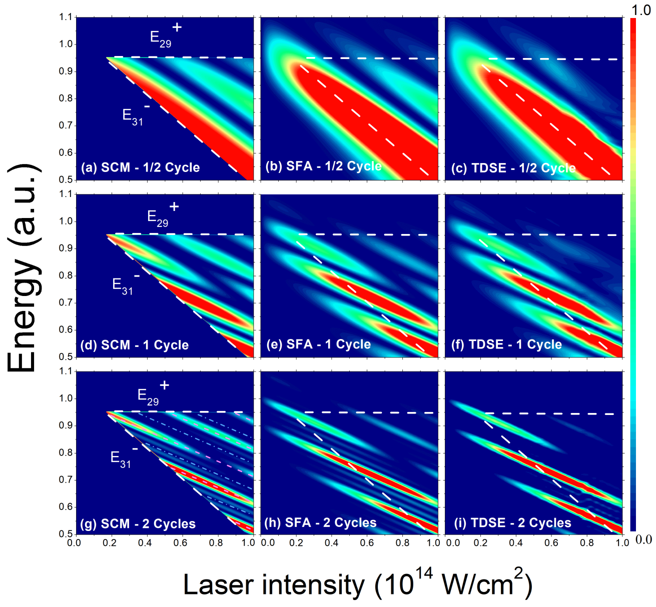

Figure 4. Photoelectron spectra in the perpendicular direction (in arbitrary units) as a function of the NIR laser intensity within the SCM [(a), (d), and (g)], the SFA [(b), (e), and (h)], and the TDSE [(c), (f), and (i)]. The XUV pulse durations are $\tau = \pi/\omega$ (a-c), $2\pi/\omega$ (d-f), and $4\pi/\omega$ (g-i). The other XUV and IR parameters are the same as in previous figures. In white dashed line we show the classical boundaries, in light-blue dotted-hashed line the frustrated SBs, i.e., E_{2m+1+n} with even $|n|$ and in magenta dashed line, the relevant SBs with odd n [Equation (16)].

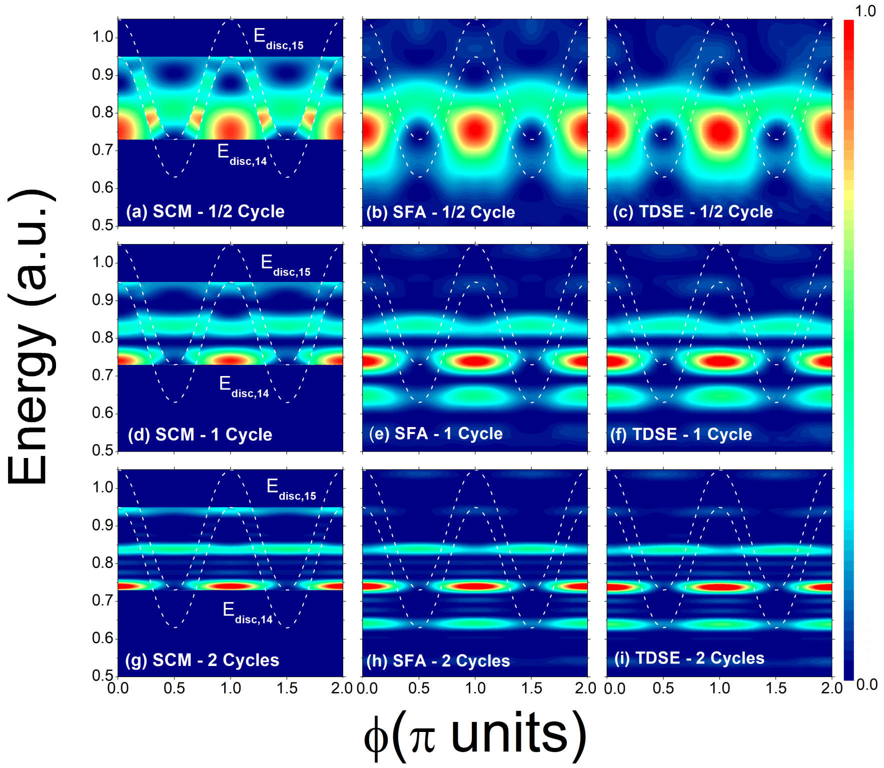

Figure 5. Photoelectron spectra in the perpendicular direction (in arbitrary units) as a function of the phase of the NIR laser ϕ within the SCM (a, d, and g), the SFA (b, e, and h), and the TDSE (c, f, and i). The XUV pulse durations are $\tau = \pi/\omega$ (a-c), $2\pi/\omega$ (d-f), and $4\pi/\omega$ (g-i). The NIR laser intensity is $I \simeq 5.62 \times 10^{13}$ W/cm^2 ($F_0 = 0.04$ a.u.). The other XUV and IR parameters are the same as in previous figures. In dashed lines we show the corresponding energy discontinuities $E_{\mathrm{disc},m} = \left[v_{0,m}^2 - A^2(\phi/\omega)\right]/2$ for T_{14} and T_{15} (see appendix B).

Finally, to scrutinize the phase delays of the sidebands as a function of the NIR intensity, Figure 6 shows the perpendicular photoelectron spectra of hydrogen for SB32, SB30, and SB28 within the SCM and SFA. The SCM reproduces all the main features of the SFA, except for SB32 out of the applicability region. At low NIR intensities, the distributions maximize at $\phi = 0$ and π, for SB30 and SB28, indicating that both sidebands are in phase, i.e., $\delta_{30} = \delta_{28} = 0$ [see Equation (26)]. Conversely, SB32 peaks at $\phi = \pi/2$ and $3\pi/2$ for low intensity with an ensuing phase delay $\delta_{32} = \pi$.

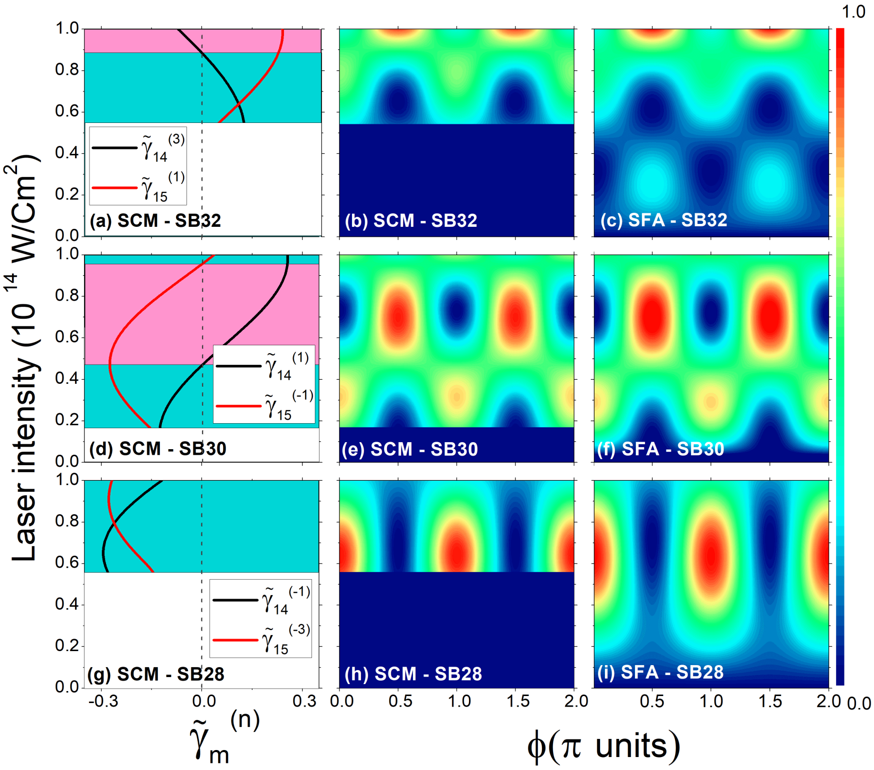

Figure 6. Photoelectron spectra for perpendicular emission as a function of the NIR laser intensity I and phase ϕ calculated within the SCM in the middle column (b, e, and h) and SFA in the right column (c, f, and i). Emission energies correspond to SB32 in (b and c), SB30 in (e and f), and SB28 in (h and i). In the left column, the normalized intrahalfcycle factor $\tilde{\gamma}_m^{(n)}$ as function of the fundamental laser intensity for energies corresponding to (a) SB32, (d) SB30, and (g) SB28. For each panel we show the intrahalfcycle factors for paths (a): $\tilde{\gamma}_{14}^{(3)}$ and $\tilde{\gamma}_{15}^{(1)}$, (d): $\tilde{\gamma}_{14}^{(1)}$ and $\tilde{\gamma}_{15}^{(-1)}$, and (g) $\tilde{\gamma}_{14}^{(-1)}$ and $\tilde{\gamma}_{15}^{(-3)}$. Cyan (magenta) regions correspond to intensity values for which the different normalized intracycle factors $\tilde{\gamma}_m^{(n)}$ have the same (opposite) sign. Pulse parameters and SFA envelope are the same as in previous figures.

The maxima of SB28 remain invariant with probe intensity (at least up to the studied intensity of 10^{14} W/cm^2), while SB32 and SB30 exhibit transitions of behavior. SB32 peaks at $\phi = 0, \pi$ for low intensities ($I \lesssim 3.16 \times 10^{13}$ W/cm^2) yielding $\delta_{32} = 0$, and at $\phi = \pi/2, 3\pi/2$ for 3.16×10^{13} W/cm$^2 \lesssim I \lesssim 8.9 \times 10^{13}$ W/cm^2 with $\delta_{32} = \pi$ and again at $\phi = 0, \pi$ for higher intensities ($I \gtrsim 8.9 \times 10^{13}$ W/cm^2) leading to $\delta_{32} = 0$. We observe that the phase delays are always either $\delta = 0$ or π depending on the relative sign of the two contributing terms $\tilde{\gamma}_{m-1}^{(n+2)}$ and $\tilde{\gamma}_m^{(n)}$, as expected from Equations (26) and (27), which is expected under strong field approximation. The model could be extended to the non-classical region by using theories that are more sophisticated, for example, the uniform saddle-point approximation [47], however, this is out of the scope of the present work.

4. Conclusions

We have developed a time-dependent nonperturbative theory of the RABBIT protocol for photoelectron emission perpendicular to the laser polarization axis. Building on our previous work for parallel emission, we generalized the semiclassical strong-field approximation by deriving analytical expressions that allow for a transparent interpretation of the phase-delay information. Our analysis shows that the perpendicular emission spectra can be factored into intrahalf- and interhalfcycle contributions or, alternatively, as intra- and intercycle contributions. In particular, we identified intrahalfcycle interference between trajectories released within the same half cycle as the main mechanism responsible for attosecond phase delays in this geometry. A distinctive feature of the perpendicular direction is the suppression of even-order sidebands, leading to a sideband spacing of 2ω, in sharp contrast to the ω spacing observed along the polarization axis. Comparisons with full SFA and the *ab initio* TDSE simulations confirm the validity of our nonperturbative semiclassical approach. The present theory thus provides a unified framework for describing attosecond chronoscopy in both parallel and perpendicular emission geometries. Future work may extend this analysis to angle-resolved photoemission and to polarization-resolved pump-probe schemes, paving the way toward a more complete understanding of attosecond electron dynamics.

Author Contributions: Conceptualization, D.G.A. and S.D.L.; methodology, M.L.O., S.D.L., and D.G.A.; software, M.L.O., M.B., S.D.L, and D.G.A.; validation, M.L.O., S.D.L, and D.G.A.; formal analysis, M.L.O. and D.G.A.; investigation, M.L.O., S.D.L, and D.G.A.; resources, S.D.L and D.G.A.; data curation, M.L.O., M.B., and S.D.L; writing—original draft preparation, D.G.A.; writing—review and editing, M.L.O., S.D.L, and D.G.A.; visualization, M.L.O.; supervision, S.D.L and D.G.A.; project administration, S.D.L and D.G.A.; funding acquisition, S.D.L and D.G.A. All authors have read and agreed to the published version of the manuscript.

Funding: This research was funded by Agencia I+D+i (Argentina) grant numbers PICT 2020-01755 and 2020-01434 and Consejo Nacional de Investigaciones Científicas y Técnicas (CONICET) (Argentina) grant number PIP 2022-2024 11220210100468CO. Programa Nacional RAICES Federal: Edición 2022 of Ministerio de Ciencia, Tecnología e Innovación (MinCyT) and PICT 2023 RAÍCES FEDERAL 01-PICT-2023-02-10 from Agencia I+D+i (Argentina).

Data Availability Statement: Data are contained in this article and can be solicited to the corresponding authors.

Acknowledgments: We gratefully acknowledge the financial support from PICT 2020-01755 and 2020-01434 of ANPCyT (Argentina), PIP 2022-2024 11220210100468CO of CONICET (Argentina), Programa Nacional RAICES Federal: Edición 2022 of Ministerio de Ciencia, Tecnología e Innovación (MinCyT) and PICT 2023 RAÍCES FEDERAL 01-PICT-2023-02-10 from ANPCyT (Argentina).

Conflicts of Interest: The authors declare no conflicts of interest.

Abbreviations

The following abbreviations are used in this manuscript:

RABBIT	Reconstruction of attosecond beating by interference of two-photon transitions
SCM	Semiclassical model
SFA	Strong-field approximation
TDSE	Time-dependent Schrodinger equation
PES	Photoelectron spectrum
HHn	High n-th order harmonic
LAPE	Laser-assisted photoionization emission
NIR	Near infrared
XUV	Extreme ultraviolet
SB	sideband

Appendix A. Dipole Moment

The z-component of the dipole element for the $1s$ state of a hydrogen atom is

$$\vec{d}(\vec{v}) = -\frac{i}{\pi} 2^{7/2} (2I_p)^{5/4} \frac{\vec{v}}{\left[v^2 + (2I_p)^2\right]^3}. \tag{A1}$$

For the case of emission along the polarization axis in Ref. [21], symmetry properties of the dipole matrix element were not taken into account. Contrarily, for perpendicular emission, it needs to be considered since according to Equation (A1), the dipole elements d_z along the polarization direction of consecutive half cycles fulfill

$$d_{m,z}\big(\hat{\rho}k + \hat{z}A(t + j\frac{\pi}{\omega})\big) = (-1)^j d_{m,z}\big(\hat{\rho}k + \hat{z}A(t)\big). \tag{A2}$$

Hence, the odd and even half cycles have opposite contributions.

Appendix B. Saddle-Point Approximation

Within the saddle-point approximation we can approximately solve the time integrals of Equation (18) yielding the addition of two (semi)classical trajectories that have been born within the same half optical cycle shown in Equation (21). The saddle times $t^{(\alpha)}$ fulfill the saddle equation $\dot{S} = dS(t^{(\alpha)})/dt = 0$, or equivalently,

$$A^2(t^{(\alpha)}) + k^2 = v_{0,m}^2 \tag{A3}$$

with $v_{0,m}^2/2 = (2m+1)\omega - I_p$, resulting in

$$\omega t^{(1)} = \mathrm{mod}\left[\sin^{-1}\left(\frac{\omega}{F_0}\beta_m^{1/2}(k)\right) - \phi, \pi\right] \tag{A4a}$$

$$\omega t^{(2)} = \mathrm{mod}\left[\pi - \sin^{-1}\left(\frac{\omega}{F_0}\beta_m^{1/2}(k)\right) - \phi, \pi\right], \tag{A4b}$$

and the weighting factor is

$$g_m(\vec{k}, t^{(\alpha)}) = \frac{\sqrt{2\pi}\, d_{z,m}\left[k\hat{\rho} + A(t^{(\alpha)})\hat{z}\right]}{\left|v_{0,m}^2 - k^2\right|^{1/4}\left|F_0\cos(\omega t^{(\alpha)} + \phi)\right|^{1/2}} \tag{A5}$$

where $\beta_m = v_{0,m}^2 - k^2$. From Equation (A3), the domain of the allowed classical trajectories perpendicular to the polarization axis is $E_{2m+1}^- \leq E \leq E_{2m+1}^+$, where $E_{2m+1}^+ = (2m+1)\omega - I_p$ and $E_{2m+1}^- = (2m+1)\omega - I_p - 2U_p$ whether $v_{0,m} \geq F_0/\omega$. The modulo function in the definition of ionization times introduces a discontinuity, which is an artifact of the SCM [31].

References

1. Kienberger, R.; Goulielmakis, E.; Uiberacker, M.; Baltuska, A.; Yakovlev, V.; Bammer, F.; Scrinzi, A.; Westerwalbesloh, T.; Kleineberg, U.; Heinzmann, U.; et al. Atomic transient recorder. *Nature* **2004**, *427*, 817–821. https://doi.org/10.1038/nature02277.
2. He, F.; Becker, A.; Thumm, U. Strong-Field Modulated Diffraction Effects in the Correlated Electron-Nuclear Motion in Dissociating H_2^+. *Phys. Rev. Lett.* **2008**, *101*, 213002. https://doi.org/10.1103/PhysRevLett.101.213002.
3. Cavalieri, A.L.; Fritz, D.M.; Lee, S.H.; Bucksbaum, P.H.; Reis, D.A.; Rudati, J.; Mills, D.M.; Fuoss, P.H.; Stephenson, G.B.; Kao, C.C.; et al. Clocking Femtosecond X Rays. *Phys. Rev. Lett.* **2005**, *94*, 114801. https://doi.org/10.1103/PhysRevLett.94.114801.
4. Paul, P.M.; Toma, E.S.; Breger, P.; Mullot, G.; Augé, F.; Balcou, P.; Muller, H.G.; Agostini, P. Observation of a Train of Attosecond Pulses from High Harmonic Generation. *Science* **2001**, *292*, 1689–1692, [https://science.sciencemag.org/content/292/5522/1689.full.pdf]. https://doi.org/10.1126/science.1059413.
5. Mauritsson, J.; Johnsson, P.; Mansten, E.; Swoboda, M.; Ruchon, T.; L'Huillier, A.; Schafer, K.J. Coherent Electron Scattering Captured by an Attosecond Quantum Stroboscope. *Phys. Rev. Lett.* **2008**, *100*, 073003. https://doi.org/10.1103/PhysRevLett.100.073003.
6. Locher, R.; Castiglioni, L.; Lucchini, M.; Greif, M.; Gallmann, L.; Osterwalder, J.; Hengsberger, M.; Keller, U. Energy-dependent photoemission delays from noble metal surfaces by attosecond interferometry. *Optica* **2015**, *2*, 405, [arXiv:cond-mat.other/1403.5449]. https://doi.org/10.1364/OPTICA.2.000405.

7. Klünder, K.; Dahlström, J.M.; Gisselbrecht, M.; Fordell, T.; Swoboda, M.; Guénot, D.; Johnsson, P.; Caillat, J.; Mauritsson, J.; Maquet, A.; et al. Publisher's Note: Probing Single-Photon Ionization on the Attosecond Time Scale [Phys. Rev. Lett. 106, 143002 (2011)]. *Phys. Rev. Lett.* **2011**, *106*, 169904. https://doi.org/10.1103/PhysRevLett.106.169904.
8. Månsson, E.P.; Sorensen, S.L.; Arnold, C.L.; Kroon, D.; Guénot, D.; Fordell, T.; Lépine, F.; Johnsson, P.; L'Huillier, A.; Gisselbrecht, M. Multi-purpose two- and three-dimensional momentum imaging of charged particles for attosecond experiments at 1 kHz repetition rate. *Review of Scientific Instruments* **2014**, *85*, 123304. https://doi.org/10.1063/1.4904372.
9. Heuser, S.; Jiménez Galán, Á.; Cirelli, C.; Marante, C.; Sabbar, M.; Boge, R.; Lucchini, M.; Gallmann, L.; Ivanov, I.; Kheifets, A.S.; et al. Angular dependence of photoemission time delay in helium. *Phys. Rev. A* **2016**, *94*, 063409. https://doi.org/10.1103/PhysRevA.94.063409.
10. Isinger, M.; Squibb, R.J.; Busto, D.; Zhong, S.; Harth, A.; Kroon, D.; Nandi, S.; Arnold, C.L.; Miranda, M.; Dahlström, J.M.; et al. Photoionization in the time and frequency domain. *Science* **2017**, *358*, 893–896, [arXiv:physics.atom-ph/1709.01780]. https://doi.org/10.1126/science.aao7043.
11. Vos, J.; Cattaneo, L.; Patchkovskii, S.; Zimmermann, T.; Cirelli, C.; Lucchini, M.; Kheifets, A.; Landsman, A.S.; Keller, U. Orientation-dependent stereo Wigner time delay and electron localization in a small molecule. *Science* **2018**, *360*, 1326–1330. https://doi.org/10.1126/science.aao4731.
12. Rudawski, P.; Harth, A.; Guo, C.; Lorek, E.; Miranda, M.; Heyl, C.M.; Larsen, E.W.; Ahrens, J.; Prochnow, O.; Binhammer, T.; et al. Carrier-envelope phase dependent high-order harmonic generation with a high-repetition rate OPCPA-system. *European Physical Journal D* **2015**, *69*, 70. https://doi.org/10.1140/epjd/e2015-50568-y.
13. Cavalieri, A.L.; Müller, N.; Uphues, T.; Yakovlev, V.S.; Baltuška, A.; Horvath, B.; Schmidt, B.; Blümel, L.; Holzwarth, R.; Hendel, S.; et al. Attosecond spectroscopy in condensed matter. *Nature* **2007**, *449*, 1029–1032. https://doi.org/10.1038/nature06229.
14. Neppl, S.; Ernstorfer, R.; Cavalieri, A.L.; Lemell, C.; Wachter, G.; Magerl, E.; Bothschafter, E.M.; Jobst, M.; Hofstetter, M.; Kleineberg, U.; et al. Direct observation of electron propagation and dielectric screening on the atomic length scale. *Nature* **2015**, *517*, 342–346. https://doi.org/10.1038/nature14094.
15. Kienberger, R.; Krausz, F. Attosecond Metrology Comes of Age. *Physica Scripta Volume T* **2004**, *110*, 32. https://doi.org/10.1238/Physica.Topical.110a00032.
16. Kazansky, A.K.; Kabachnik, N.M. On the gross structure of sidebands in the spectra of laser-assisted Auger decay. *Journal of Physics B: Atomic, Molecular and Optical Physics* **2010**, *43*, 035601.
17. Maquet, A.; Taïeb, R. Two-colour IR+XUV spectroscopies: the "soft-photon approximation". *Journal of Modern Optics* **2007**, *54*, 1847–1857, [http://dx.doi.org/10.1080/09500340701306751]. https://doi.org/10.1080/09500340701306751.
18. Dahlström, J.M.; Guénot, D.; Klünder, K.; Gisselbrecht, M.; Mauritsson, J.; L'Huillier, A.; Maquet, A.; Taïeb, R. Theory of attosecond delays in laser-assisted photoionization. *Chemical Physics* **2013**, *414*, 53–64. https://doi.org/10.1016/j.chemphys.2012.01.017.
19. Maquet, A.; Caillat, J.; Taïeb, R. Attosecond delays in photoionization: time and quantum mechanics. *Journal of Physics B Atomic Molecular Physics* **2014**, *47*, 204004. https://doi.org/10.1088/0953-4075/47/20/204004.
20. Bivona, S.; Bonanno, G.; Burlon, R.; Gurrera, D.; Leone, C. Signature of quantum interferences in above-threshold detachment of negative ions by a short infrared pulse. *Phys. Rev. A* **2008**, *77*, 051404. https://doi.org/10.1103/PhysRevA.77.051404.
21. López, S.D.; Ocello, M.L.; Arbó, D.G. Time-dependent theory of reconstruction of attosecond harmonic beating by interference of multiphoton transitions. *Phys. Rev. A* **2024**, *110*, 013104, [arXiv:physics.atom-ph/2401.04299]. https://doi.org/10.1103/PhysRevA.110.013104.
22. Gramajo, A.A.; Della Picca, R.; Garibotti, C.R.; Arbó, D.G. Intra- and intercycle interference of electron emissions in laser-assisted XUV atomic ionization. *Phys. Rev. A* **2016**, *94*, 053404, [arXiv:physics.atom-ph/1605.07457]. https://doi.org/10.1103/PhysRevA.94.053404.
23. Lewenstein, M.; You, L.; Cooper, J.; Burnett, K. Quantum field theory of atoms interacting with photons: Foundations. *Phys. Rev. A* **1994**, *50*, 2207–2231. https://doi.org/10.1103/PhysRevA.50.2207.
24. Corkum, P.; Perry, M.D. Physics with intense laser pulses. *Optics & Photonics News* **1993**, *4*, 52–53.
25. Arbó, D.G.; Miraglia, J.E.; Gravielle, M.S.; Schiessl, K.; Persson, E.; Burgdörfer, J. Coulomb-Volkov approximation for near-threshold ionization by short laser pulses. *Physical Review A* **2008**, *77*, 013401. https://doi.org/10.1103/PhysRevA.77.013401.

26. Kazansky, A.K.; Sazhina, I.P.; Kabachnik, N.M. Angle-resolved electron spectra in short-pulse two-color XUV+IR photoionization of atoms. *Phys. Rev. A* **2010**, *82*, 033420. https://doi.org/10.1103/PhysRevA.82.033420.
27. Bivona, S.; Bonanno, G.; Burlon, R.; Leone, C. Two-color ionization of hydrogen by short intense pulses. *Laser Physics* **2010**, *20*, 2036–2044. https://doi.org/10.1134/S1054660X10190023.
28. Arbó, D.G.; Ishikawa, K.L.; Schiessl, K.; Persson, E.; Burgdörfer, J. Intracycle and intercycle interferences in above-threshold ionization: The time grating. *Phys. Rev. A* **2010**, *81*, 021403(R). https://doi.org/10.1103/PhysRevA.81.021403.
29. Arbó, D.G.; Ishikawa, K.L.; Schiessl, K.; Persson, E.; Burgdörfer, J. Diffraction at a time grating in above-threshold ionization: The influence of the Coulomb potential. *Phys. Rev. A* **2010**, *82*, 043426. https://doi.org/10.1103/PhysRevA.82.043426.
30. Gramajo, A.A.; Della Picca, R.; López, S.D.; Arbó, D.G. Intra- and intercycle interference of angle-resolved electron emission in laser-assisted XUV atomic ionization. *Journal of Physics B Atomic Molecular Physics* **2018**, *51*, 055603. https://doi.org/10.1088/1361-6455/aaaa28.
31. Gramajo, A.A.; Della Picca, R.; Arbó, D.G. Electron emission perpendicular to the polarization direction in laser-assisted XUV atomic ionization. *Phys. Rev. A* **2017**, *96*, 023414, [arXiv:physics.atom-ph/1703.09585]. https://doi.org/10.1103/PhysRevA.96.023414.
32. Korneev, P.A.; Popruzhenko, S.V.; Goreslavski, S.P.; Yan, T.M.; Bauer, D.; Becker, W.; Kübel, M.; Kling, M.F.; Rödel, C.; Wünsche, M.; et al. Interference Carpets in Above-Threshold Ionization: From the Coulomb-Free to the Coulomb-Dominated Regime. *Physical Review Letters* **2012**, *108*, 223601. https://doi.org/10.1103/PhysRevLett.108.223601.
33. Korneev, P.A.; Popruzhenko, S.V.; Goreslavski, S.P.; Becker, W.; Paulus, G.G.; Fetić, B.; Milošević, D.B. Interference structure of above-threshold ionization versus above-threshold detachment. *New Journal of Physics* **2012**, *14*, 055019. https://doi.org/10.1088/1367-2630/14/5/055019.
34. Maxwell, A.S.; Figueira de Morisson Faria, C.; Lai, X.; Sun, R.; Liu, X. Spiral-like holographic structures: Unwinding interference carpets of Coulomb-distorted orbits in strong-field ionization. *Phys. Rev. A* **2020**, *102*, 033111. https://doi.org/10.1103/PhysRevA.102.033111.
35. Tong, X.M.; Chu, S.I. Theoretical study of multiple high-order harmonic generation by intense ultrashort pulsed laser fields: A new generalized pseudospectral time-dependent method. *Chem. Phys.* **1997**, *217*, 119–130.
36. Tong, X.M.; Chu, S.I. Time-dependent approach to high-resolution spectroscopy and quantum dynamics of Rydberg atoms in crossed magnetic and electric fields. *Phys. Rev. A* **2000**, *61*, 031401(R). https://doi.org/10.1103/PhysRevA.61.031401.
37. Tong, X.M.; Lin, C.D. Empirical formula for static field ionization rates of atoms and molecules by lasers in the barrier-suppression regime. *Journal of Physics B: Atomic, Molecular and Optical Physics* **2005**, *38*, 2593.
38. Macri, P.A.; Miraglia, J.E.; Grabielle, M.S.; Colavecchia, F.D.; Garibotti, C.R.; Gasaneo, G. Theory with correlations for ionization in ion-atom collisions. *Physical Review A* **1998**, *57*, 2223–2226. https://doi.org/10.1103/PhysRevA.57.2223.
39. Wolkow, D. Uber eine Klasse von Lösungen der Diracschen Gleichung. *Zeitschrift für Physik* **1935**, *94*, 250–260. https://doi.org/10.1007/BF01331022.
40. Picca, R.D.; Fiol, J.; Fainstein, P.D. Factorization of laser-pulse ionization probabilities in the multiphotonic regime. *Journal of Physics B: Atomic, Molecular and Optical Physics* **2013**, *46*, 175603. https://doi.org/10.1088/0953-4075/46/17/175603.
41. Della Picca, R.; Ciappina, M.F.; Lewenstein, M.; Arbó, D.G. Laser-assisted photoionization: Streaking, sideband, and pulse-train cases. *Phys. Rev. A* **2020**, *102*, 043106. https://doi.org/10.1103/PhysRevA.102.043106.
42. López, S.D.; Otranto, S.; Garibotti, C.R. Double ionization of He by ion impact: Second-order contributions to the fully differential cross section. *Phys. Rev. A* **2014**, *89*, 062709. https://doi.org/10.1103/PhysRevA.89.062709.
43. Arbó, D.G.; Dimitriou, K.I.; Persson, E.; Burgdörfer, J. Sub-Poissonian angular momentum distribution near threshold in atomic ionization by short laser pulses. *Phys. Rev. A* **2008**, *78*, 013406. https://doi.org/10.1103/PhysRevA.78.013406.
44. Véniard, V.; Taïeb, R.; Maquet, A. Two-Color Multiphoton Ionization of Atoms Using High-Order Harmonic Radiation. *Physical Review Letters* **1995**, *74*, 4161–4164. https://doi.org/10.1103/PhysRevLett.74.4161.

45. Véniard, V.; Taïeb, R.; Maquet, A. Phase dependence of (N+1)-color (N > 1) ir-uv photoionization of atoms with higher harmonics. *Phys. Rev. A* **1996**, *54*, 721–728. https://doi.org/10.1103/PhysRevA.54.721.
46. Guenot, D.; Klünder, K.; Arnold, C.L.; Kroon, D.; Dahlström, J.M.; Miranda, M.; Fordell, T.; Gisselbrecht, M.; Johnsson, P.; Mauritsson, J.; et al. Photoemission-time-delay measurements and calculations close to the 3 s-ionization-cross-section minimum in ar. *Physical Review A* **2012**, *85*, 053424. https://doi.org/https://doi.org/10.1103/PhysRevA.85.053424.
47. Figueira de Morisson Faria, C.; Schomerus, H.; Becker, W. High-order above-threshold ionization: The uniform approximation and the effect of the binding potential. *Phys. Rev. A* **2002**, *66*, 043413. https://doi.org/10.1103/PhysRevA.66.043413.